Available online at www.sciencedirect.com
SCIENCE DIRECT®
ELSEVIER
International Journal of Solids and Structures 41 (2004) 7267–7285
INTERNATIONAL JOURNAL OF SOLIDS and STRUCTURES
www.elsevier.com/locate/ijsolstr

Unit cell debonding analyses for arbitrary orientation of plastic anisotropy

Brian Nyvang Legarth *

Department of Mechanical Engineering, Solid Mechanics, Technical University of Denmark, Nils Koppels Allé, Building 404, DK-2800 Kgs. Lyngby, Denmark

Received 21 June 2004
Available online 14 August 2004

Abstract

Debonding of rigid inclusions embedded in the elastic–plastic aluminum alloy Al 2090-T3 is analyzed numerically using a unit cell model taking full account of finite strains. The cell is subjected to overall biaxial plane strain tension and periodical boundary conditions are applied to represent arbitrary orientations of plastic anisotropy. Plastic anisotropy is considered using two phenomenological anisotropic yield criteria, namely Hill [Proceedings of the Royal Society of London A 193 (1948) 281] and Barlat et al. [International Journal of Plasticity 7 (1991) 693]. For this material plastic anisotropy delays debonding compared to plastic isotropy except for the case of Hill's yield function when the tensile directions coincided with the principal axes of anisotropy. For some inclinations of the principal axes of anisotropy relative to the tensile directions, the stress strain responses are identical but the deformation modes are mirror images of each other.

Keywords: Finite strain; Plastic anisotropy; Periodical boundary conditions; Debonding

1. Introduction

Reinforcement of metals by adding brittle second phase particles is used to improve the material properties, for instance stiffness, tensile strength and creep resistance (see McDanels, 1985). However, some negative side effects, such as poor ductility and low fracture toughness, are observed due to void nucleation and growth along the particle–matrix interface or even particle breakage (Divecha et al., 1981).

* Corresponding author. Tel.: +45 4525 4257; fax: +45 4593 1475.
E-mail address: brian@mek.dtu.dk

0020-7683/$ - see front matter © 2004 Elsevier Ltd. All rights reserved.
doi:10.1016/j.ijsolstr.2004.06.051

A lot of work has been done to gain better understanding on this subject. Some work assumed perfectly bonded particles (Christman et al., 1989a,b; Tvergaard, 1990a; Bao et al., 1991); but also debonding and breakage have been modeled (Nutt and Needleman, 1987; Tvergaard, 1990b, 1995). For the purpose of studying debonding Needleman (1987) proposed a phenomenological cohesive zone model, in which the relative normal separation of the particle and the matrix material determines failure. The model was generalized by Tvergaard (1990b) to also account for tangential separation. Most studies have applied conventional plasticity models or lately a non-local plasticity model (Niordson and Tvergaard, 2002), but also a single crystal plasticity model has been used (Xu and Needleman, 1993).

Texture is a major cause of orientation dependent material response for the plastic range of deformation. This is called plastic anisotropy, and only very few debonding analyses have taken plastic anisotropy into account. Legarth (2003) has used a unit cell model to investigate particle debonding in geometrically or plastically anisotropic materials, where the geometrical anisotropy is induced by the shape and the spacing of the inclusions. For the particular material considered, debonding was significantly promoted by using the classical anisotropic yield function proposed by Hill (1948, 1950), compared to conventional isotropic plasticity. The study was extended to include four different anisotropic yield functions in addition to the isotropic von Mises yield surface, and also a non-normality flow rule was included (Legarth and Kuroda, in press). Both the maximum load carrying capacity and the failure strain were found to be highly affected by the yield criterion applied.

In both studies (Legarth, 2003; Legarth and Kuroda, in press) the initial orientation of plastic anisotropy was restricted to coincide with the tensile directions, due to the symmetry boundary conditions used for the unit cell. For arbitrary initial orientation of plastic anisotropy shear stresses may develop in a non-symmetric manner on the cell boundaries, leading to a wavy deformation of the cell edges. The present paper releases any restrictions on the orientation of plastic anisotropy, as periodical boundary conditions are adopted for a unit cell representing periodically distributed rigid inclusions embedded in an elastic–viscoplastic metal. The cell is subjected to biaxial plane strain tension. Plastic anisotropy is modeled using two different phenomenological yield functions, either Hill (1948, 1950) or Barlat et al. (1991). Additionally, the particle–matrix interface strength is allowed to have a periodical variation along the circumference of the inclusion.

2. Problem formulation

A general study of materials containing inclusions would require a full three-dimensional analysis in order to describe the geometry of the inclusions as well as the plastic anisotropy with any orientation. However, as progressive interface debonding occurs in the present study, such an analysis would be complicated and time consuming. For some problems the geometry and the arrangement of the inclusions can be well approximated by the axisymmetric assumption as done by Tvergaard (1990b), but plastic anisotropy is usually not well described by such an approximation. Therefore, plane strain modeling is chosen here since this is expected to give a good representation of the plastic anisotropy, but the geometry of the inclusions cannot be modeled as accurately as in the axisymmetric assumption.

We assume periodically distributed rigid inclusions with elliptical cross sections embedded in a homogeneous matrix material, Fig. 1(a). When analyzing the problem, a biaxially loaded unit cell containing a single inclusion is adopted, as shown in Fig. 1(b). At the center of the inclusion a fixed Cartesian coordinate system, x_i, is located, aligned with the cell edges. The angle between x_i and the orthonormal basis, $\mathbf{n}_i$, defining the principal axes of plastic anisotropy, $\hat{x}_i$, is denoted θ. The out of plane axis, x_3, is taken to be identical with $\hat{x}_3$. For arbitrary initial values of θ the initially straight edges of the cell would not remain straight during the deformation. Thus, periodical boundary conditions are needed to ensure compatibility as well as force equilibrium across the cell edges. The boundary conditions are here formulated on the basis of

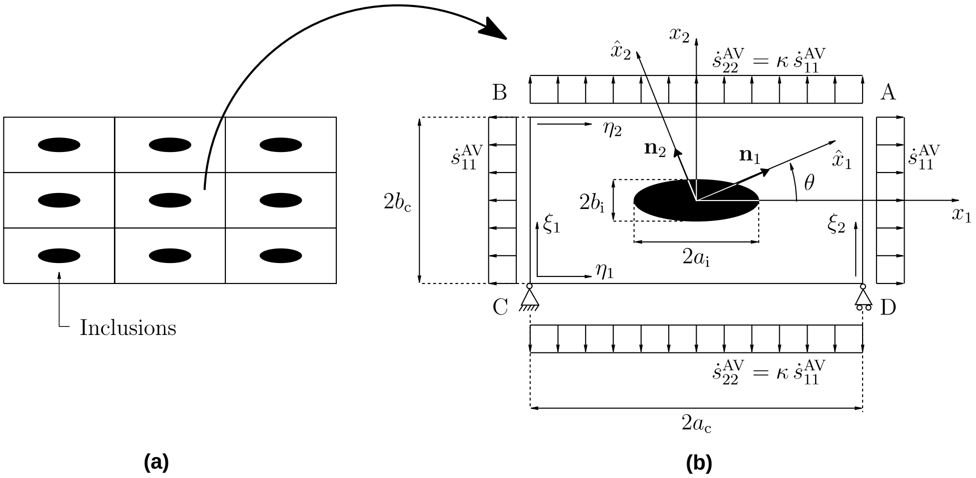

Fig. 1. The plane strain cell model for rigid elliptical inclusions: (a) Assumed periodically arranged inclusions in the overall inhomogeneous material; (b) The cell used for modeling is shown with initial dimensions, loads, supports and coordinate systems.

incremental quantities. In terms of the length measuring coordinates, η_i and ξ_i, see Fig. 1(b), the displacement increments on the cell sides, $\dot{u}_i$, are therefore constrained as

$$\begin{aligned} \dot{u}_1(\eta_1) &= \dot{u}_1(\eta_2) - \dot{u}_1^{\mathrm{B}} \quad \text{and} \quad \dot{u}_2(\eta_1) = \dot{u}_2(\eta_2) - \dot{u}_2^{\mathrm{B}} \\ \dot{u}_1(\xi_1) &= \dot{u}_1(\xi_2) - \dot{u}_1^{\mathrm{D}} \quad \text{and} \quad \dot{u}_2(\xi_1) = \dot{u}_2(\xi_2) - \dot{u}_2^{\mathrm{D}} \end{aligned} \tag{1}$$

where $(\,\dot{}\,)$ is the time rate, $\frac{\mathrm{d}}{\mathrm{d}t}(\ )$, and $\dot{u}_i^{\mathrm{B}}$ and $\dot{u}_i^{\mathrm{D}}$ are the displacements at the two cell corners B and D, respectively, see Fig. 1(b). It is noted that the support in corner C is automatically satisfied using Eq. (1). Force equilibrium is formulated in terms of the nominal surface tractions, T_i

$$\begin{aligned} \dot{T}_1(\eta_1) &= -\dot{T}_1(\eta_2) \quad \text{and} \quad \dot{T}_2(\eta_1) = -\dot{T}_2(\eta_2) \\ \dot{T}_1(\xi_1) &= -\dot{T}_1(\xi_2) \quad \text{and} \quad \dot{T}_2(\xi_1) = -\dot{T}_2(\xi_2) \end{aligned} \tag{2}$$

The conditions stated in Eqs. (1) and (2) hold for the microscopic cell problem in Fig. 1(b). However, some conditions for the macroscopic average problem, denoted by $(\ )^{\mathrm{AV}}$, must also be satisfied. These constraints represent the overall conditions implied by the testing equipment and are here chosen to be

$$\dot{F}_{11}^{\mathrm{AV}} = \frac{\Delta_1}{\Delta t} \quad \left(\dot{u}_1^{\mathrm{D}} = \frac{\Delta_1}{\Delta t}\right) \tag{3}$$

$$\dot{F}_{21}^{\mathrm{AV}} = 0 \quad (\dot{u}_2^{\mathrm{D}} = 0) \tag{4}$$

$$\dot{s}_{22}^{\mathrm{AV}} = \kappa \dot{s}_{11}^{\mathrm{AV}} \tag{5}$$

and one of

$$\begin{cases} \dot{s}_{21}^{\mathrm{AV}} = 0 \quad \text{or} \\ \dot{F}_{12}^{\mathrm{AV}} = 0 \quad (\dot{u}_1^{\mathrm{B}} = 0) \end{cases} \tag{6}$$

Here, $F_{ij}^{\mathrm{AV}} \neq F_{ji}^{\mathrm{AV}}$ are the average deformation gradients, Δ_1 is a displacement increment quantity, Δt the time step and $s_{ij}^{\mathrm{AV}} \neq s_{ji}^{\mathrm{AV}}$ are the average 1st Piola–Kirchhoff stresses. The condition in Eq. (4) means that the cell edges initially parallel with the x_1-axis may curve locally, within the cell, but on the average these edges remain straight and do not rotate. Initially, $F_{ij}^{AV} = 0$ and $s_{ij}^{AV} = 0$. Thus, average values remain zero during the loading if the increments are prescribed to be zero. Most of the results will be presented for $s_{21}^{AV} = 0$, but the effect of applying $F_{12}^{AV} = 0$ instead of $s_{21}^{AV} = 0$ will also be shown. Finally, the microscopic cell problem is related to the macroscopic average problem through force equilibrium

$$\int_A \dot{T}_i \,\mathrm{d}A = \int_{A^{AV}} \dot{T}_i^{AV} \,\mathrm{d}A^{AV} \tag{7}$$

The integrations are performed at the cell edges and the tractions are related to s_{ij} by

$$T_i = s_{ji} n_j; \quad T_i^{AV} = s_{ji}^{AV} n_j^{AV} \tag{8}$$

where n_j is the outward unit normal to the cell edge in the reference state. Since we here will use the updated Lagrangian formulation, see McMeeking and Rice (1975), in which the current deformed configuration is chosen as the reference state, T_i and n_j are identical to the tractions per unit current surface area and the unit normal to the current surface, respectively. In this situation the 1st Piola–Kirchhoff stress equals the Cauchy stress, $\sigma_{ij} = s_{ij}$, but of course $\dot{\sigma}_{ij}$ is not equal to $\dot{s}_{ij}$.

The main tensile direction is taken to be the x_1-direction meaning that $0 \leqslant \kappa < 1$. Finally, the initial dimensions of the cell are $(2a_c, 2b_c)$ and the cross section of the inclusion is given by $(2a_i, 2b_i)$, see Fig. 1(b). The initial volume fraction of the inclusion is then $f = \pi a_i b_i/(4a_c b_c)$.

3. Material model

3.1. Anisotropic plasticity model

In rate form the kinematics of the matrix material is assumed to be written as, see Dafalias (1985a,b, 1993)

$$\begin{aligned} \mathbf{D} &= \mathbf{D}^{e} + \mathbf{D}^{p} \\ \mathbf{W} &= \boldsymbol{\omega} + \mathbf{W}^{p} \\ \mathbf{L} &= \mathbf{D} + \mathbf{W} \end{aligned} \tag{9}$$

taking full account of small elastic and finite plastic strains. The bold symbol notation is used to indicate tensors. The symmetric part of the velocity gradient tensor, $\mathbf{L}$, is the strain rate, $\mathbf{D}$, and the anti-symmetric part is the continuum spin tensor, $\mathbf{W}$. The superscripts e and p denote the elastic and plastic parts, respectively, and $\boldsymbol{\omega}$ is the spin of the substructure, whereas $\mathbf{W}^{p}$ is the plastic spin. The objective rate with respect to $\boldsymbol{\omega}$, $(\overset{\triangledown}{\ })$, of the Cauchy stress or the true stress, $\boldsymbol{\sigma}$, is given as

$$\overset{\triangledown}{\boldsymbol{\sigma}} = \dot{\boldsymbol{\sigma}} - \boldsymbol{\omega}\boldsymbol{\sigma} + \boldsymbol{\sigma}\boldsymbol{\omega} = \mathbf{C} : \mathbf{D}^{e} = \mathbf{C} : (\mathbf{D} - \mathbf{D}^{p}) \tag{10}$$

Here, $\mathbf{C}$ are the isotropic elastic moduli determined by Young's modulus E and Poisson's ratio v. The plastic response of the material is assumed to be viscous with anisotropic yield surfaces invoked through the quantity $J(\hat{\sigma}_{ij})$, where the stress components with respect to the orthotropic axes are $\hat{\sigma}_{ij} = \mathbf{n}_i \cdot \boldsymbol{\sigma} \cdot \mathbf{n}_j$ for $i,j = 1, 2, 3$. The hardening is isotropic. The plastic strain increments, $\mathbf{D}^{p}$, are then given as

$$\mathbf{D}^{p} = \dot{\phi}\mathbf{N}^{p}; \quad \dot{\phi} = \dot{\epsilon}_0 \left(\frac{J}{g}\right)^{1/m}; \quad \mathbf{N}^{p} = \frac{\partial J}{\partial \boldsymbol{\sigma}} \tag{11}$$

Here $\dot{\epsilon}_0$ is a reference strain rate, m is a strain rate sensitivity parameter and $g = g(\epsilon^{\mathrm{p}})$ is a deformation dependent power law function

$$g(\epsilon^{\mathrm{p}}) = \sigma_0\left(1 + \frac{\epsilon^{\mathrm{p}}}{\epsilon_0}\right)^n; \quad \epsilon^{\mathrm{p}} = \int \dot{\epsilon}^{\mathrm{p}}\,\mathrm{d}t; \quad \dot{\epsilon}^{\mathrm{p}} = \dot{\phi}\sqrt{\frac{2}{3}\mathbf{N}^{\mathrm{p}} : \mathbf{N}^{\mathrm{p}}} \tag{12}$$

where σ_0 is the initial uniaxial yield stress, $\epsilon_0 = \sigma_0/E$ and n is the hardening exponent. The plastic part of the spin tensor is assumed to be described as (Dafalias, 1984; Zbib and Aifantis, 1988; Kuroda, 1995–1997)

$$\mathbf{W}^{\mathrm{p}} = \frac{a}{J}(\boldsymbol{\sigma}\mathbf{D}^{\mathrm{p}} - \mathbf{D}^{\mathrm{p}}\boldsymbol{\sigma}) \tag{13}$$

where a is the plastic spin coefficient. For plastically isotropic materials the principal axes of $\boldsymbol{\sigma}$ and $\mathbf{D}^{\mathrm{p}}$ coincide and the plastic spin vanishes. Here plane strain modeling is considered. Therefore $\hat{\sigma}_{13} = \sigma_{13}$ and $\hat{\sigma}_{23} = \sigma_{23}$ will always be zero. In this finite strain formulation the orthonormal basis is allowed to rotate during the deformation, and since the orthotropic axes are attached to the substructure of the material, the evolution law becomes

$$\overset{\triangledown}{\mathbf{n}}_i = \dot{\mathbf{n}}_i - \boldsymbol{\omega}\mathbf{n}_i \equiv 0 \Rightarrow \dot{\mathbf{n}}_i = \boldsymbol{\omega}\mathbf{n}_i, \quad \mathbf{n}_1 = \begin{Bmatrix} \cos(\theta) \\ \sin(\theta) \end{Bmatrix} \tag{14}$$

The initial orientation of plastic anisotropy is denoted by θ_0.

Plastic anisotropy is modeled using two different phenomenological theories, namely Hill (1948, 1950), which is quadratic in terms of the stress components, and the non-quadratic proposal by Barlat et al. (1991), subsequently referred as Hill-48 and Barlat-91, respectively.

3.1.1. Hill-48

The classical quadratic yield criterion proposed by Hill (1948, 1950) is

$$\begin{aligned} J = {} & \sqrt{\frac{3}{2(F+G+H)}}[F(\hat{\sigma}_{22} - \hat{\sigma}_{33})^2 + G(\hat{\sigma}_{33} - \hat{\sigma}_{11})^2 + H(\hat{\sigma}_{11} - \hat{\sigma}_{22})^2 + 2N\hat{\sigma}_{12}^2 \\ & + 2L\hat{\sigma}_{23}^2 + 2M\hat{\sigma}_{13}^2]^{1/2} - C_1 g(\epsilon^{\mathrm{p}})\left(\frac{\dot{\phi}}{\dot{\epsilon}_0}\right)^m = 0 \\ C_1 = {} & \sqrt{\frac{3(G+H)}{2(F+G+H)}} \end{aligned} \tag{15}$$

When the coefficients of anisotropy are chosen to be $F = G = H = 1$ and $N = L = M = 3$ the yield function simplifies to the isotropic von Mises yield criterion.

3.1.2. Barlat-91

Based on the work of Hershey (1954) and Hosford (1972), Barlat et al. (1991) proposed the higher order yield function

$$\begin{aligned} J &= \left(\frac{\Phi}{2}\right)^{1/d} - g(\epsilon^{\mathrm{p}})\left(\frac{\dot{\phi}}{\dot{\epsilon}_0}\right)^m = 0 \\ \Phi &= [S_1 - S_2]^d + [S_2 - S_3]^d + [S_1 - S_3]^d \end{aligned} \tag{16}$$

where, see Barlat et al. (1997)

$$
\begin{aligned}
S_1 &= 2\sqrt{I_2}\cos\left(\frac{\bar{\theta}}{3}\right)\\
S_2 &= 2\sqrt{I_2}\cos\left(\frac{\bar{\theta}-2\pi}{3}\right)\\
S_3 &= 2\sqrt{I_2}\cos\left(\frac{\bar{\theta}+2\pi}{3}\right)
\end{aligned}
\tag{17}
$$

$$
\begin{aligned}
I_2 &= \tfrac{1}{3}[(\bar{f}\overline{F})^2 + (\bar{g}\overline{G})^2 + (\bar{h}\overline{H})^2] + \tfrac{1}{54}[(\bar{a}\overline{A} - \bar{c}\overline{C})^2 + (\bar{c}\overline{C} - \bar{b}\overline{B})^2 + (\bar{b}\overline{B} - \bar{a}\overline{A})^2]\\
I_3 &= \tfrac{1}{54}[(\bar{c}\overline{C} - \bar{b}\overline{B})(\bar{a}\overline{A} - \bar{c}\overline{C})(\bar{b}\overline{B} - \bar{a}\overline{A})] + \bar{f}\bar{g}\bar{h}\overline{F}\overline{G}\overline{H}\\
&\quad - \tfrac{1}{6}[(\bar{c}\overline{C} - \bar{b}\overline{B})(\bar{f}\overline{F})^2 + (\bar{a}\overline{A} - \bar{c}\overline{C})(\bar{g}\overline{G})^2 + (\bar{b}\overline{B} - \bar{a}\overline{A})(\bar{h}\overline{H})^2]
\end{aligned}
\tag{18}
$$

$$
0 \leqslant \bar{\theta} = \arccos\left(\frac{I_3}{I_2^{3/2}}\right) \leqslant \pi
\tag{19}
$$

with

$$
\begin{aligned}
\overline{A} &= \hat{\sigma}_{22} - \hat{\sigma}_{33}; \quad \overline{F} = \hat{\sigma}_{23}\\
\overline{B} &= \hat{\sigma}_{33} - \hat{\sigma}_{11}; \quad \overline{G} = \hat{\sigma}_{31}\\
\overline{C} &= \hat{\sigma}_{11} - \hat{\sigma}_{22}; \quad \overline{H} = \hat{\sigma}_{12}
\end{aligned}
\tag{20}
$$

For $\bar{\theta} = 0$ or $\bar{\theta} = \pi$ in Eq. (19) the derivatives in Eq. (11) are singular. For these particular cases Eq. (16) reduces to

$$
\Phi = 2 \cdot 3^d I_2^{\frac{d}{2}} \quad \text{for } \bar{\theta} = 0 \text{ or } \bar{\theta} = \pi
\tag{21}
$$

which are then directly used to evaluate the strain increments. If the coefficients of anisotropy, $\bar{a}$, $\bar{b}$, $\bar{c}$, $\bar{f}$, $\bar{g}$ and $\bar{h}$, are chosen to be unity and the exponent to $d = 2$, this criterion reduces to the von Mises yield surface.

3.2. The cohesive zone model

The fracture process at the particle–matrix interface is analyzed using the cohesive zone model proposed by Tvergaard (1990b), which takes normal as well as tangential interfacial separation into account, u_n and u_t, respectively. The model is a phenomenological model, which represents the average effect of debonding mechanisms on a somewhat larger length scale than atomic.

A non-dimensional parameter, λ, describing the separation of the matrix material from the inclusion is defined as

$$
\lambda = \sqrt{\left(\frac{u_n}{\delta_n}\right)^2 + \left(\frac{u_t}{\delta_t}\right)^2}
\tag{22}
$$

In pure normal separation, $u_t = 0$, the interface tractions vanish when $u_n \geqslant \delta_n$ and in pure tangential separation, $u_n = 0$, the interface tractions vanish when $u_t \geqslant \delta_t$. The tractions are given by

$$
T_n = \frac{u_n}{\delta_n}F(\lambda); \quad T_t = \gamma\frac{u_t}{\delta_t}F(\lambda)
\tag{23}
$$

where the function $F(\lambda)$ is

$$F(\lambda) = \frac{27}{4}\sigma_{\max}(1 - 2\lambda + \lambda^2); \quad 0 \leqslant \lambda \leqslant 1 \tag{24}$$

For a uniform interfacial strength along the circumference of the inclusion debonding would initiate simultaneously at $x_1 = \pm a_i$ as $0 \leqslant \kappa < 1$ in Eq. (5), see Fig. 1. This complicates the numerical analyses a great deal as will be discussed in section 4. In order to overcome such difficulties the maximum interfacial stress, $\sigma_{\max}$, is here realistically modeled with an imperfection

$$\sigma_{\max} = \bar{\sigma}_{\max}[1 - A_i \cos(w_i + \varphi_i)] \tag{25}$$

where $\bar{\sigma}_{\max}$ is the mean value of the maximum interfacial stress, whereas A_i and φ_i are the amplitude and the phase, respectively, of the imperfection, and w_i is the counterclockwise angle relative to the x_1-axis for a point at the interface. For pure normal separation the maximum stress is $\sigma_{\max}$ (at $u_n = \frac{1}{3}\delta_n$) and the work of fracture per unit interface area is $9\sigma_{\max}\delta_n/16$. Similarly, in pure tangential separation the maximum stress is $\gamma\sigma_{\max}$ (at $u_t = \frac{1}{3}\delta_t$) and the work of fracture is $9\gamma\sigma_{\max}\delta_t/16$. The model requires six parameters ($\delta_n, \delta_t, \gamma, \bar{\sigma}_{\max}, A_i$ and φ_i), and total debonding will occur when $\lambda = 1$. Further details, including the incremental form of the model, are provided by Tvergaard (1990b).

In order to satisfy force and moment equilibrium with the cohesive interface during the deformation, the inclusion will translate and, in some cases with plastic anisotropy, also rotate. A point on the inclusion surface is given by w_i and the distance from the center of the inclusion, $R(w_i)$ (where for instance $R(0) = a_i$ and $R(\pi/2) = b_i$). Additionally, the counterclockwise angle from the x_2-axis to the tangent of the surface point considered is denoted by θ_i. Thus, force and moment equilibrium for the inclusion are

$$\begin{aligned}
&\int_{S_\mathrm{I}} \{T_n \cos(\theta_i) - T_t \sin(\theta_i)\}\,\mathrm{d}S = 0 \\
&\int_{S_\mathrm{I}} \{T_n \sin(\theta_i) + T_t \cos(\theta_i)\}\,\mathrm{d}S = 0 \\
&\int_{S_\mathrm{I}} R(w_i)\{T_n \sin(\theta_i - w_i) + T_t \cos(\theta_i - w_i)\}\,\mathrm{d}S = 0
\end{aligned} \tag{26}$$

where S_I is the debonding interface. For an inclusion with circular cross section ($a_i/b_i = 1$) $\theta_i = w_i$ and moment equilibrium is simple

$$\int_{S_\mathrm{I}} a_i T_t\,\mathrm{d}S = \int_{S_\mathrm{I}} b_i T_t\,\mathrm{d}S = 0 \tag{27}$$

The three displacements corresponding to the movement of the inclusion are then introduced through the relative openings u_n and u_t.

4. Numerical procedure

Disregarding body forces the incremental form of the principle of virtual work in an updated Lagrangian (or Eulerian) formulation, see McMeeking and Rice (1975), becomes (Yamada and Hirakawa, 1978; Tvergaard, 1990b; Yamada and Sasaki, 1995)

$$\begin{aligned}
&\Delta t \int_V \dot{s}_{ij}\delta v_{j,i}\,\mathrm{d}V + \Delta t \int_{S_\mathrm{I}} (\dot{T}_n \delta\dot{u}_n + \dot{T}_t \delta\dot{u}_t)\,\mathrm{d}S \\
&\quad = \Delta t \int_S \dot{T}_i, \delta v_i\,\mathrm{d}S - \left[\int_V s_{ij}\delta v_{j,i}\,\mathrm{d}V - \int_S T_i \delta v_i\,\mathrm{d}S + \int_{S_\mathrm{I}} (T_n \delta\dot{u}_n + T_t \delta\dot{u}_t)\,\mathrm{d}S\right]
\end{aligned} \tag{28}$$

where all integrations are carried out in the deformed configuration. The volume is denoted V and the surface by S, whereas δv_i are the virtual velocities in the current deformed configuration. The bracketed term in

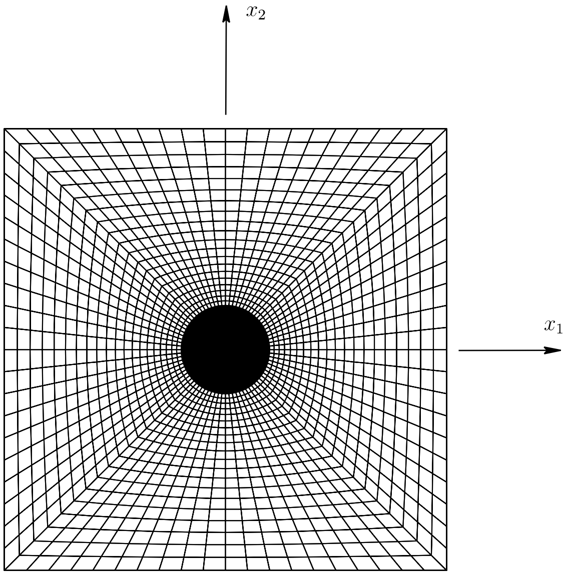

Fig. 2. The finite element mesh applied. The volume fraction is $f = 0.03$ and the cell geometry is given by $a_c/b_c = 1$ and $a_i/b_i = 1$.

Eq. (28) is the equilibrium correction term needed due to numerical errors. If, however, the current state satisfies equilibrium, the term vanishes. A finite element method based on Eq. (28) is employed, using the finite element mesh shown in Fig. 2. Since the inclusion is assumed to be rigid only the matrix material is discretized. The mesh consist of 1600 quadrilaterals, each subdivided into four constant strain (linear displacement) triangles.

During debonding neither the load increment nor the increment in F_{11}^{AV} are useful as the prescribed quantity, since both may change sign along the equilibrium path. By combining the finite element procedure with a Rayleigh–Ritz method this kind of numerical problems can be treated. The technique is developed by Tvergaard (1976) where a general discussion of the subject can be found. The basic idea is to be able to prescribe quantities that are known to be increasing. Here, the method is also used to implement the periodical boundary condition, Eqs. (1)–(6), as well as Eq. (26), by choosing all nodal displacements at the cell boundary and the particle–matrix interface in addition to the three degrees of freedom of the particle as unknowns in the combined Rayleigh–Ritz method. Thus, during debonding the condition in Eq. (3) is substituted to prescribe an increasing interfacial separation instead. As this methodology only allows for prescribing one degree of freedom at the time it excludes the possibility of representing simultaneous debonding initiation at $x_1 = \pm a_i$, see Fig. 1. In order to avoid such failure modes the non-uniform interfacial strength is prescribed, Eq. (25), leading to initial debonding either at $x_1 = +a_i$ or $x_1 = -a_i$ depending on the values of A_i and φ_i. At the same time this imperfection appears to be quite realistic.

The deformation history is calculated in a linear incremental manner. In order to increase the stable time step, Δt, at any time, t, the rate tangent modulus method is used, see Peirce et al. (1984). This is a forward gradient method based on an estimate of the plastic strain rate in the interval between t and $t + \Delta t$.

5. Numerical results

Geometrical anisotropy is present if the aspect ratio of the cell, a_c/b_c, or the principal axes of the elliptic cross section of the inclusion, a_i/b_i, differ from unity. This study will focus on plastic anisotropy and therefore geometrical isotropy is assumed, i.e. $a_c/b_c = a_i/b_i = 1$, with the volume fraction $f = 0.03$.

The overall average stress strain response of the cell will be evaluated and it is taken as the true stress component, σ_1, versus the logarithmic strain, ϵ_1, in the main tensile direction, x_1. The quantities are calculated as

$$\sigma_1 = \frac{1}{2b_c + \Delta b_c^{\mathrm{A}}} \int_{-b_c}^{b_c+\Delta b_c^{\mathrm{A}}} [T_1]_{x_1=a_c+\Delta a_c^{\mathrm{D}}}\, \mathrm{d}x_2; \quad \epsilon_1 = \ln\left(1 + \frac{\Delta a_c^{\mathrm{D}}}{2a_c}\right) \tag{29}$$

where Δa_c^{D} and Δb_c^{A} are the accumulated elongations of the cell in the main tensile direction and in the transverse direction, respectively. The cell is loaded such that $\kappa = 0.5$. The matrix material is aluminum alloy 2090-T3 with the assumed material parameters $m = 0.005$, $n = 0.1$, $\dot{\epsilon}_0 = 0.002\ \mathrm{s}^{-1}$, $\nu = 0.3$, $\epsilon_0 = 0.005$ and $\sigma_0/E = 0.005$. For this alloy Barlat et al. (2003) provide the experimental data used when calibrating the two yield functions considered here, see Table 1. Here it is chosen to apply information about σ_0/σ_0, σ_{45}/σ_0, σ_{90}/σ_0 and r_0 ($\equiv D_{22}/D_{33}$ for $\theta_0 = 0°$) when calibrating the yield functions. As suggested by Logan and Hosford (1980) the exponent d in Eq. (16) is eight. Although realistic values of the plastic spin coefficient, a, depend upon the intensity of anisotropy, the values of a less than 10, have yielded acceptable predictions of the behavior in large plastic shear deformations (Kuroda, 1997, 1999). Thus, here we will consider $a = 10$. However, it should be noted that negative values of the plastic spin coefficient may be necessary if experimental data are to be fitted (Dafalias, 2000), or theoretical dissipation requirements are to be satisfied (Levitas, 1998). The interface stiffness is given by $\delta_n = \delta_t = 0.02a_i = 0.02b_i$, $\gamma = 1$, $\bar{\sigma}_{\max} = 3\sigma_0$ and $\varphi_i = 0°$. The effect of different values of the imperfection amplitude, A_i in Eq. (25), on the average stress strain response is investigated and the results are shown in Fig. 3 for the case of isotropic matrix material (vanishing plastic spin) and $s_{21}^{\mathrm{AV}} = 0$. The sudden stress drop indicates the point of debonding initiation, where the stress in the region near the interface has reached the critical interfacial stress. It is noted that both increments of ϵ_1 and σ_1 become negative. Fig. 3 shows as expected, that the magnitude of A_i does not affect the material response as long as debonding is absent. Large values of A_i cause a part of the interface to be much weaker than the rest of the interface, leading to earlier onset of debonding as shown for $A_i = 0.1$. As the magnitude of A_i approaches zero the interface becomes uniform and Fig. 3 then shows that the overall strain for debonding converges at $\epsilon_1 \simeq 0.055$ when $A_i = 0.001$. If $A_i > 0$ the strongest part of the interface occurs for $x_1 < 0$, while for $A_i < 0$ the highest interfacial stress occurs for $x_1 > 0$. However, interchanging the sign of A_i has no effect on the average stress strain response due to the interfacial symmetry ($\varphi_i = 0°$), but the deformed configuration is changed. This is shown in Fig. 4 for $A_i = \pm 0.01$ at $\epsilon_1 = 0.07$ in Fig. 3. The inclusion is still bonded on its left hand side for $A_i = +0.01$, Fig. 4(a), whereas the right hand side is bonded for $A_i = -0.01$, Fig. 4(b). In the following analyses, the imperfection is assumed to be given by $A_i = 0.01$ (and $\varphi_i = 0°$).

In Fig. 5 the average stress strain responses are shown in the case of plastically anisotropic matrix material with different initial orientations of the axes of anisotropy, θ_0. The isotropic result with $A_i = 0.01$ from Fig. 3 is also repeated in Fig. 5, and the degree of anisotropy is as specified in Table 1. Fig. 5(a) displays the solutions obtained using the quadratic yield function Hill-48, whereas Fig. 5(b) provides the results when Barlat-91 is adopted. In these analyses the stress state is rather complex since only $\sigma_{13} = \sigma_{23} = 0$. However, as analytically shown by Legarth et al. (2002) for a non-hardening ($n = 0$) Hill-48 material, the yield stress in full plane strain tension varies periodically for any set of the coefficients of anisotropy, and has the same

Table 1
Coefficients used for Al 2090-T3 in the two yield functions

Experimental data	$\sigma_0/\sigma_0 = 1.00$, $\sigma_{45}/\sigma_0 = 0.81$, $\sigma_{90}/\sigma_0 = 0.91$, $r_0 = 0.21$
Hill-48	$F = 5.96$, $G = 4.76$, $H = 1$, $N = 12.2$
Barlat-91	$d = 8$, $\bar{a} = 1.34$, $\bar{b} = 1.17$, $\bar{c} = 0.81$, $\bar{h} = 1.23$

Experimental data are taken from Barlat et al. (2003).

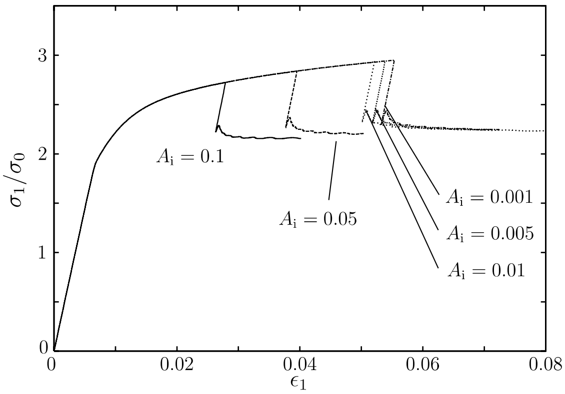

Fig. 3. Effects of imperfection in the interfacial stress, σ_{max}, Eq. (25), on the overall average stress strain response of the cell for isotropic matrix material (vanishing plastic spin) and $s_{21}^{AV} = 0$. The sudden stress drop indicates the point of debonding initiation.

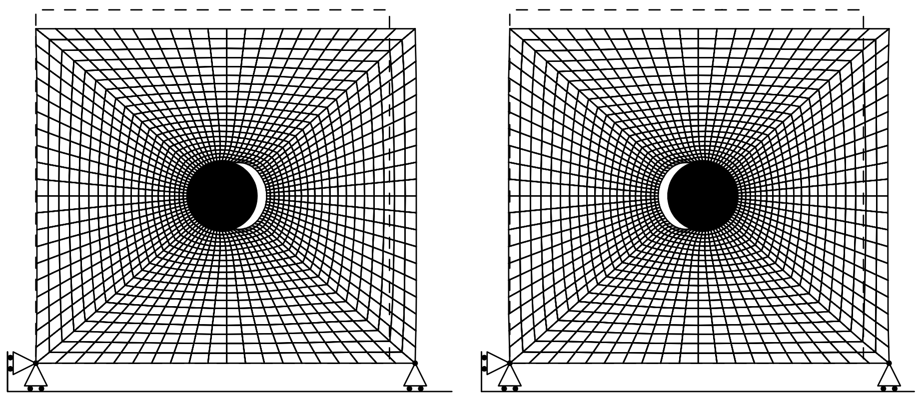

Fig. 4. Deformed configurations for isotropic matrix materials (vanishing plastic spin) taken at the overall strain $\epsilon_1 = 0.07$, see Fig. 3. The undeformed geometry is shown by the dashed line: (a) $A_i = +0.01$ (see Fig. 3); (b) $A_i = -0.01$.

values at the four orientations $\pm\theta_0$ and $\pm(90° - \theta_0)$. Minimum and maximum values are obtain for $\theta_0 = 45° + 90°z$ and $\theta_0 = 90°z$ with $z = [\ldots, -1, 0, 1, \ldots]$, respectively. It must be emphasized that initial yielding occurs before full plane strain yielding (Legarth et al., 2002). Thus, the stress strain curves in plane strain tension, for instance for $\theta_0 = 0°$ and 90°, differ at initial plastic yielding, but the difference decays when the condition of plastic plane strain deformation, $D_{33}^{p} = 0$, is approached. Similar conclusions can be obtained numerically for Barlat-91. In Fig. 5 this behavior is recognized, since the results for $\theta_0 = 0°$ and 22.5° practically coincide with the results for $\theta_0 = 90°$ and 67.5°, respectively, for both yield criteria. At these orientations the rotation of the inclusion, Ψ, is zero for $\theta_0 = 0°$ and 90° but when $\theta_0 = 22.5°$ or 67.5°, Ψ has the same magnitude with opposite signs, i.e. $\Psi \simeq -2.5°$ for $\theta_0 = 22.5°$ and $\Psi \simeq +2.5°$ for $\theta_0 = 67.5°$ in the load range investigated. For a high yield stress (for this complex stress state) a large fraction of the critical interfacial stress, σ_{max}, will be generated in the elastic range and debonding will occur after a relatively small amount of deformation, as shown in Fig. 5 for $\theta_0 = 0°$ and 90°. As the yield stress decreased, larger overall deformation is required in order to generate stresses near the inclusion high

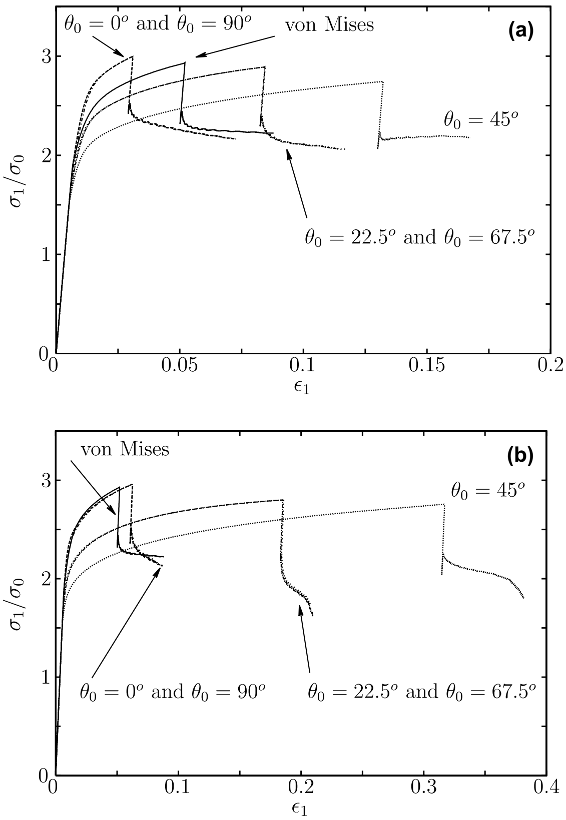

Fig. 5. Stress strain responses for anisotropic plasticity in the matrix material with $A_i = 0.01$, $a = 0$ and $s_{21}^{AV} = 0$. The sudden stress drop indicates the point of debonding initiation: (a) Hill-48; (b) Barlat-91.

enough to initiate debonding. This effect is seen in Fig. 5 for $\theta_0 = 22.5°$ and 45°. The anisotropic response for $\theta_0 = 0°$ or 90° using Hill-48, Fig. 5(a), is the only result that predict an overall failure strain, $\epsilon_1 \simeq 0.03$, smaller than the isotropic result, $\epsilon_1 \simeq 0.05$. All other anisotropic results yield a softer response and consequently delayed debonding. For Hill-48 the latest debonding occurs for $\epsilon_1 \simeq 0.13$, and for Barlat-91 the latest debonding occurs for $\epsilon_1 \simeq 0.32$ (both for $\theta_0 = 45°$). The maximum stress level is seen to be reduced as the flow stress reduces, from $\sigma_1/\sigma_0 \simeq 3.0$ for $\theta_0 = 0°$ (and $\theta_0 = 90°$) to $\sigma_1/\sigma_0 \simeq 2.7$ for $\theta_0 = 45°$.

For selected overall strains, ϵ_1 in Fig. 5, contours of constant effective plastic strain, ϵ^p, are shown in the deformed configuration in Figs. 6 and 7 using Hill-48 and Barlat-91, respectively. Figs. 6(a) and 7(a) display the results for $\theta_0 = 22.5°$, while Figs. 6(b) and 7(b) show the solutions when $\theta_0 = 67.5°$ and 45°, respectively. The undeformed configuration is shown by the dashed line. The wavy deformation of the cell boundary is observed, Figs. 6 and 7(a). For $\theta_0 = 45°$ some symmetry occurs between x_i and $\hat{x}_i$ resulting in straight cell edges during the deformation as shown in Fig. 7(b). The average stress strain responses for $\theta_0 = 22.5°$ and 67.5° using Hill-48 were found to be practically identical, Fig. 5(a), but Fig. 6 shows that the deformation mode for $\theta_0 = 67.5°$ is the mirror image with respect to a line parallel with the x_1-axis of the deformation mode for $\theta_0 = 22.5°$. Same characteristics are seen when Barlat-91 is considered, but this is not shown in the paper. In addition, the boundary condition $F_{21}^{AV} = 0$ causes the upper and lower cell edges to remain nearly straight during the deformation. The contours of effective plastic strain in Fig. 6 show finite plastic deformation, $\epsilon^p \gtrsim 0.2$, even though the overall straining is relatively low, $\epsilon_1 = 0.08$. For the configurations

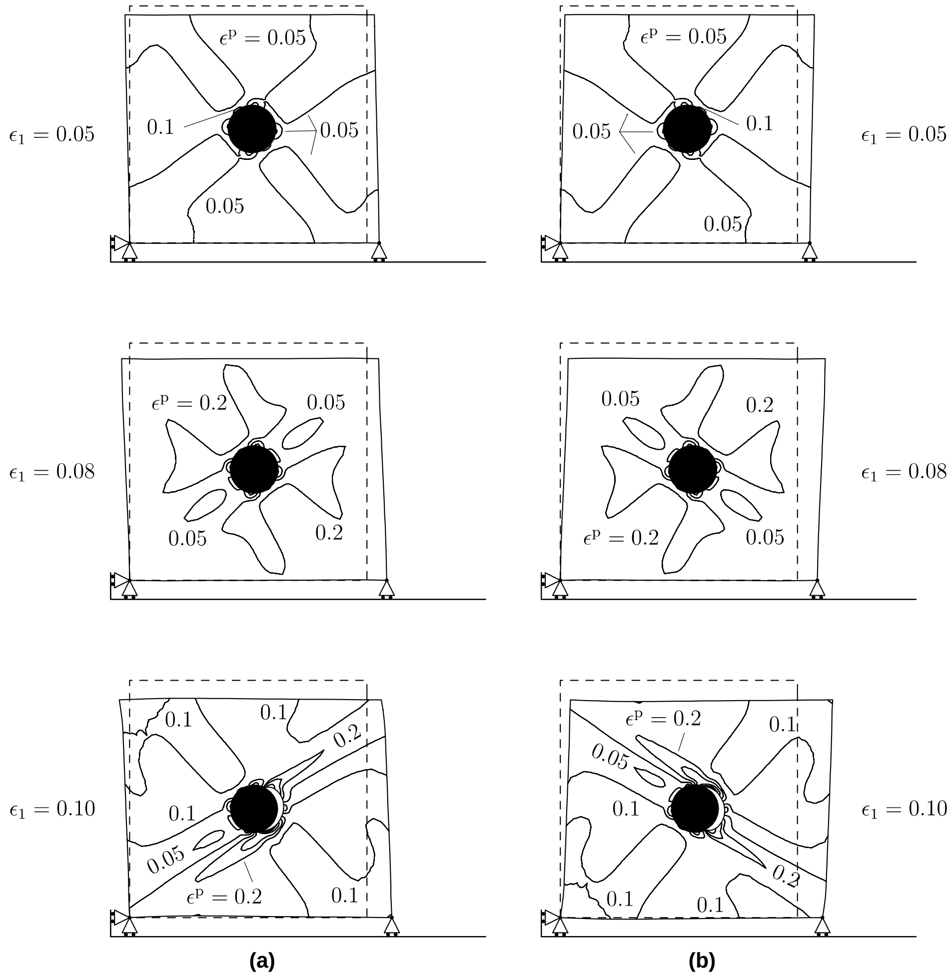

Fig. 6. Deformed configurations with contours of effective plastic strain, ϵ^p, taken at different overall strain levels using Hill-48, see Fig. 5(a). The undeformed geometry is shown by the dashed line: (a) $\theta_0 = 22.5°$; (b) $\theta_0 = 67.5°$.

where debonding has occurred, $\epsilon_1 = 0.1$ in Fig. 6 and $\epsilon_1 = 0.2$ or $\epsilon_1 = 0.35$ in Fig. 7, the contours illustrate intensive plastic deformation in the region near the void. Especially at the tip of the void, where the inclusion is still bonded, high gradients of the effective plastic strain are found, indicating progressive void growth due to further debonding.

To illustrate the periodical boundary conditions Fig. 8 shows a cluster consisting of nine deformed cells where a void has nucleated. The configuration is taken at $\epsilon_1 = 0.20$ using Barlat-91 with $\theta_0 = 22.5°$, see also Fig. 7(a). It is seen that the boundary conditions ensure compatibility.

Effects of the plastic spin ($a = 10$ in Eq. (13)) on the overall stress strain response are provide in Fig. 9. The cell and the material parameters as well as the boundary conditions are as specified for the results presented in Fig. 5. The response for the von Mises material shown in Fig. 5 is repeated in Fig. 9 as this result is unaffected by the plastic spin. In the case of a material without inclusions were the principal axes of anisotropy are initially coaxial with the tensile directions, $\theta_0 = 0°$ and 90°, the plastic spin would vanish. However, as inclusions are present and the principal axes of anisotropy rotate according to Eq. (14) as the defor-

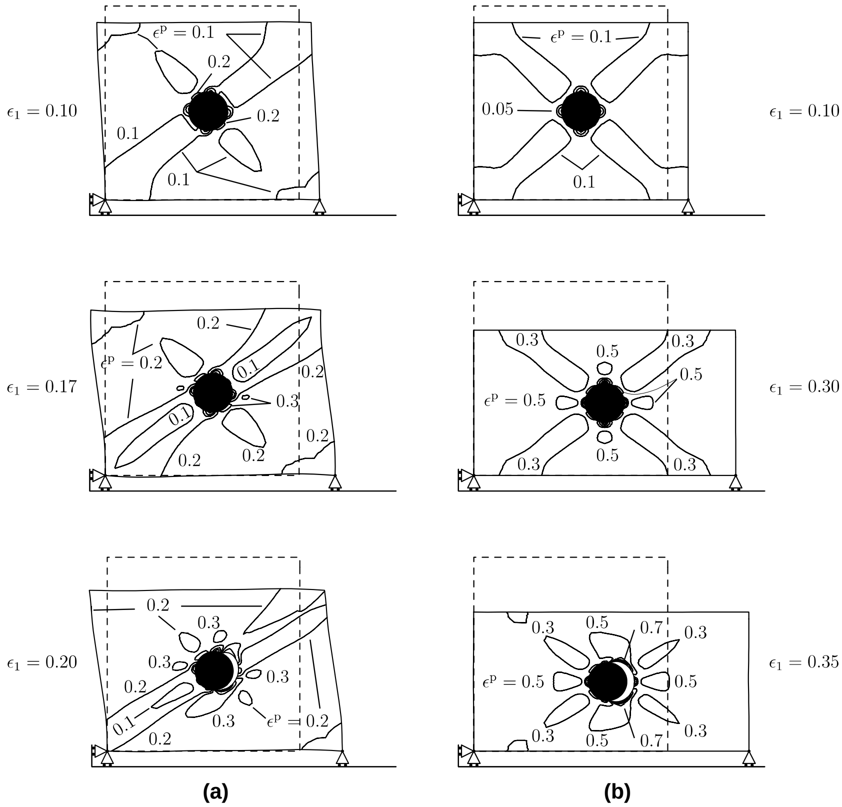

Fig. 7. Deformed configurations with contours of effective plastic strain, ϵ^p, taken at different overall strain levels using Barlat-91, see Fig. 5(b). The undeformed geometry is shown by the dashed line: (a) $\theta_0 = 22.5°$; (b) $\theta_0 = 45°$.

mations continue, non-vanishing plastic spin terms result. In the cases of Hill-48 with $\theta_0 = 0°$ and 90° without plastic spin, Fig. 5(a), debonding initiates at the overall strain $\epsilon_1 \simeq 0.03$. At this straining θ has evolved very little and therefore initiation of debonding with plastic spin accounted for takes place at $\epsilon_1 \simeq 0.03$ as well, Fig. 9(a). For Barlat-91 without plastic spin debonding initiates at $\epsilon_1 \simeq 0.063$, Fig. 5(b). At this state of deformation non-vanishing plastic spin occurs and failure in the Barlat-91 material with plastic spin is therefore found to be slightly promoted, such that debonding occurs at the smaller strain $\epsilon_1 \simeq 0.060$, Fig. 9(b). When the deformation proceeds after initial debonding, the average stress, σ_1/σ_0, is found to be higher in the plastic spin material compared to the material without plastic spin. Thus, for Hill-48 with $\theta_0 = 0°$ and 90° the average stress at $\epsilon_1 = 0.075$ is increased from $\sigma_1/\sigma_0 \simeq 2.20$ to $\sigma_1/\sigma_0 \simeq 2.25$, as seen by comparison of Figs. 5(a) and 9(a). The same holds for the Barlat-91 material. For the cases were the principal axes of anisotropy do not initially coincide with the tensile directions, $\theta_0 = 22.5°$, 45° and 67.5°, the predicted failure strain is found to be reduced for both Hill-48 and Barlat-91 due to the plastic spin. Thus, for $\theta_0 = 22.5°$ and 67.5° debonding initiation occurs at $\epsilon_1 \simeq 0.04$ for Hill-48 and at $\epsilon_1 \simeq 0.08$ for Barlat-91 if plastic spin is accounted for, Fig. 9, but at $\epsilon_1 \simeq 0.09$ for Hill-48 and at $\epsilon_1 \simeq 0.18$ for Barlat-91 if plastic spin is neglected, Fig. 5. At the intermediate initial orientation of plastic anisotropy, $\theta_0 = 45°$, the plastic spin causes debonding to occur at $\epsilon_1 \simeq 0.10$ for Hill-48 and at $\epsilon_1 \simeq 0.15$ for Barlat-91, Fig. 9, which is significantly earlier than that of the corresponding cases without plastic spin, $\epsilon_1 \simeq 0.13$ for Hill-48 and at $\epsilon_1 \simeq 0.32$ for Barlat-91, Fig. 5.

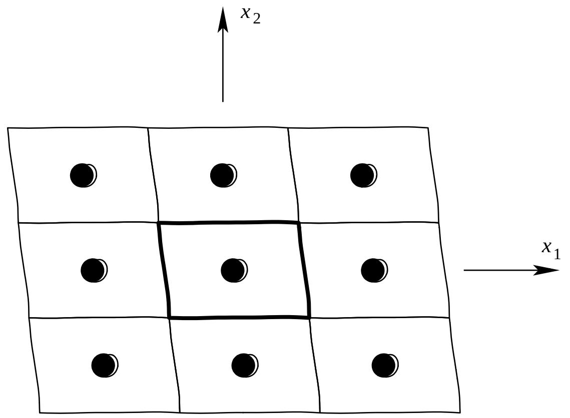

Fig. 8. A cluster of deformed cells taken at $\epsilon_1 = 0.20$ using Barlat-91 with $\theta_0 = 22.5°$, see Fig. 7(a). The cell used for the computations is shown by the thick line at the center.

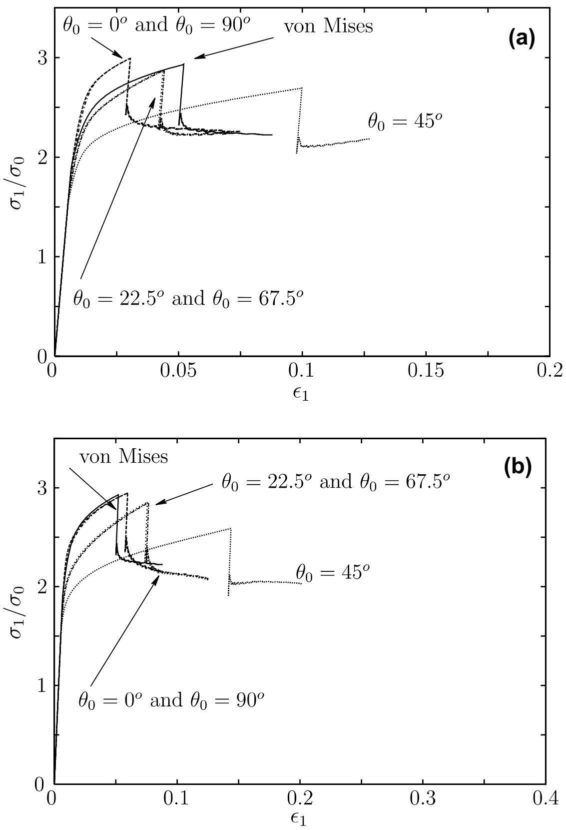

Fig. 9. Stress strain responses for anisotropic plasticity in the matrix material with $A_i = 0.01$, $a = 10$ and $s_{21}^{AV} = 0$. The sudden stress drop indicates the point of debonding initiation: (a) Hill-48; (b) Barlat-91.

The previous results are obtained using the boundary condition $s_{21}^{AV}=0$. However, depending on the experimental setup the boundary condition $F_{12}^{AV}=0$ may as well apply and Fig. 10 provides the average stress strain responses using $F_{12}^{AV}=0$ in Eq. (6) with zero plastic spin, $a=0$ in Eq. (13). The Hill-48 material is shown in Fig. 10(a) and the Barlat-91 material is shown in Fig. 10(b). The isotropic result is also shown in both diagrams. As expected, the response for the isotropic von Mises material is found to be identical with the results obtained for the boundary condition $s_{21}^{AV}=0$, Fig. 5, since both boundary conditions are automatically fulfilled due to symmetry if plastic anisotropy is absent. Even if plastic anisotropy is taken into account both $s_{21}^{AV}=0$ and $F_{12}^{AV}=0$ are satisfied for $\theta_0=0°$, 90°. Thus, for these orientations and the two yield functions considered here no difference between the two boundary conditions in Eq. (6) are seen on the average stress strain responses, Figs. 5 and 10. Fig. 7(b) illustrates that $F_{12}^{AV}=0$ is practically also fulfilled for $\theta_0=45°$, with $s_{21}^{AV}=0$ prescribed, and the corresponding stress strain response is therefore found to be identical for the two boundary conditions considered, as seen by comparison of Figs. 5 and 10. When $s_{21}^{AV}=0$, the two solutions for $\theta_0=22.5°$ and 67.5° were found to be practically identical for Hill-48 as well as Barlat-91, Fig. 5. If $F_{12}^{AV}=0$, this similarity still holds, but now the applied boundary condition play a role, since $F_{12}^{AV}=0$ is not automatically satisfied, see Figs. 6 and 7(a). As seen by comparison of Figs. 5 and 10 for $\theta_0=22.5°$ and 67.5°, debonding occurs earlier when $F_{12}^{AV}=0$ is applied. For Hill-48 debonding occurs at $\epsilon_1\simeq 0.08$ for $s_{21}^{AV}=0$, Fig. 5(a), and at $\epsilon_1\simeq 0.06$ for $F_{12}^{AV}=0$, Fig. 10(a). Similarly, for Barlat-91 debonding occurs at $\epsilon_1\simeq 0.19$ for $s_{21}^{AV}=0$, Fig. 5(b), but already at $\epsilon_1\simeq 0.11$ for $F_{12}^{AV}=0$, Fig. 10(b).

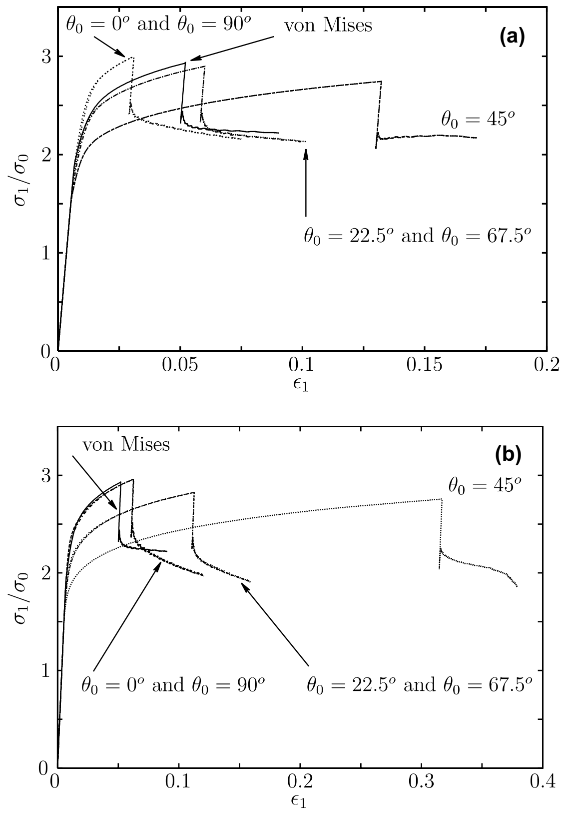

Fig. 10. Stress strain response for anisotropic plasticity in the matrix material with $A_i=0.01$, $a=0$ and $F_{12}^{AV}=0$. The sudden stress drop indicates the point of debonding initiation: (a) Hill-48; (b) Barlat-91.

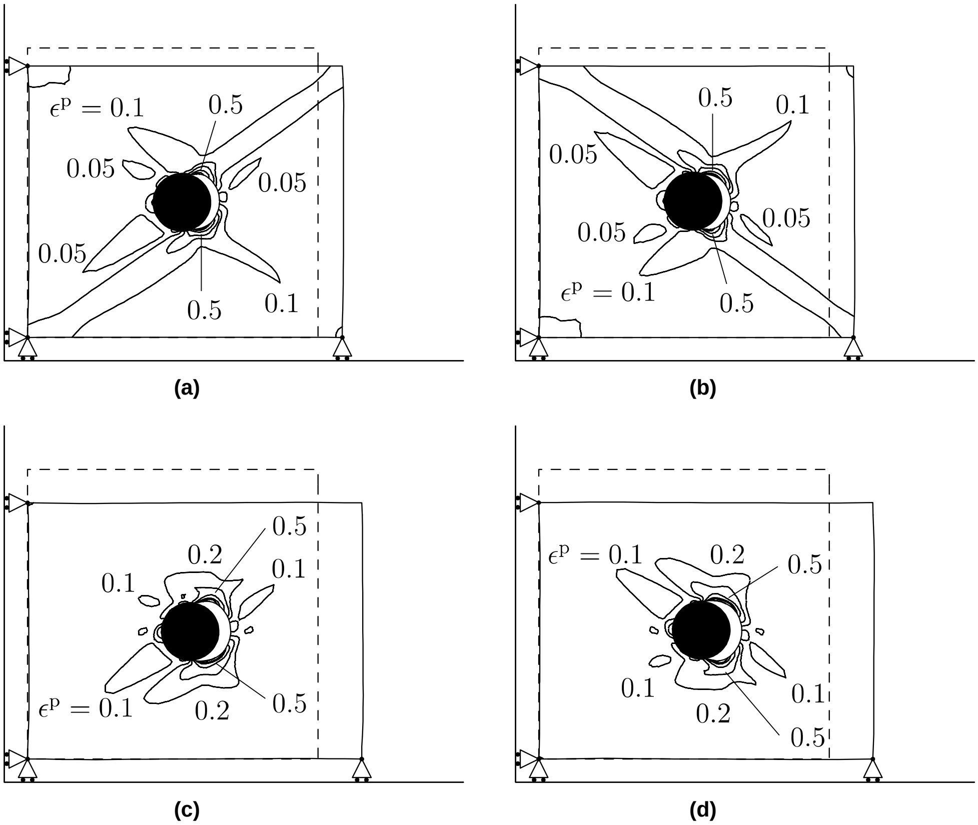

Fig. 11. Deformed cells with contours of effective plastic strain using the boundary condition $F_{12}^{AV} = 0$, see Fig. 10: (a) Hill-48 for $\theta_0 = 22.5°$ at $\epsilon_1 = 0.08$; (b) Hill-48 for $\theta_0 = 67.5°$ at $\epsilon_1 = 0.08$; (c) Barlat-91 for $\theta_0 = 22.5°$ at $\epsilon_1 = 0.14$; (d) Barlat-91 for $\theta_0 = 67.5°$ at $\epsilon_1 = 0.14$.

The stress level, σ_1/σ_0, is slightly increased if the boundary condition $F_{12}^{AV} = 0$ is applied. For Hill-48 at $\epsilon_1 = 0.06$ the stress level is $\sigma_1/\sigma_0 \simeq 2.8$ for $s_{21}^{AV} = 0$ and $\sigma_1/\sigma_0 \simeq 2.9$ for $F_{12}^{AV} = 0$, as seen by comparison of Figs. 5(a) and 10(a). At $\epsilon_1 = 0.10$ for Barlat-91 the stress level is $\sigma_1/\sigma_0 \simeq 2.7$ for $s_{21}^{AV} = 0$ and $\sigma_1/\sigma_0 \simeq 2.8$ for $F_{12}^{AV} = 0$, see Figs. 5(b) and 10(b).

Contours of effective plastic strain, ϵ^p, in deformed geometries using Hill-48 and Barlat-91 at $\epsilon_1 = 0.08$ and 0.14, respectively, are shown in Fig. 11 for $\theta_0 = 22.5°$ and 67.5°, see also Fig. 10. For this set of symmetric boundary conditions on the average configuration ($F_{12}^{AV} = F_{21}^{AV} = 0$) the contours of ϵ^p are found to be non-symmetric. It is also seen that the complication of using periodical boundary conditions is not very critical since the cell edges almost remain straight, but of course periodical boundary conditions are very important if $s_{21}^{AV} = 0$, as shown for instance in Fig. 8.

6. Discussion

A unit cell model containing a single rigid inclusion is used to investigate failure arising from debonding at the particle–matrix interface. The cell is quadratic and subjected to biaxial plane strain tension and the cross section of the inclusion is assumed to be circular. The overall average stress strain is evaluated and debonding is observed as a sudden stress drop at a certain failure strain.

Debonding is described by a cohesive zone model (Tvergaard, 1990b), which is modified to also account for some interfacial imperfection. The imperfection is modeled by a cosine-variation of the maximum interfacial stress along the circumference of the inclusion. As the amplitude of the imperfection approaches zero the interface becomes uniform and the predicted failure strain, ϵ_1, approaches a specific value depending on the material parameters. For isotropic material behavior using the cell shown in Fig. 2 the failure strain is found to approach $\epsilon_1 \simeq 0.055$, Fig. 3.

The main focus in the paper is on the effects of plastically anisotropic matrix material formulated by two different phenomenological yield criteria, namely the classical proposal by Hill (1948, 1950) and a later proposal by Barlat et al. (1991). A fundamental difference between these two functions is the exponent on the stress components, as Hill's proposal is quadratic whereas Barlat's is non-quadratic. However, the exponent of the latter depends on the crystal structure of the material considered. Thus, for BCC-configurations the exponent is six but eight for FCC-structures, as recommended by Hosford (1980). For arbitrary initial orientations of the principal axes of plastic anisotropy, θ_0, initially straight edges of the cell will deform in some wavy deformation mode as shear stresses may developed in a non-symmetric manner across the cell boundaries. This is handled by applying periodical boundary conditions for the cell, ensuring compatibility as well as force equilibrium across the cell edges, see for instance Fig. 8. Due to some periodicity with respect to θ_0 in the plane strain yield stress, results obtained for $\theta_0 = 0°$ and 22.5° are practically identical with the results for $\theta_0 = 90°$ and 67.5°, respectively, for both yield criteria. Compared to plastically isotropic matrix material, the plastic anisotropy considered here predicts softer responses leading to debonding at higher overall straining, Fig. 5. However, using the quadratic yield function with $\theta_0 = 0°$ (or $\theta_0 = 90°$) debonding is promoted. Even though the stress strain responses for $\theta_0 = 22.5°$ and 67.5° are similar, the corresponding deformation modes are mirror images with respect to the main tensile direction, see Fig. 6. Effects of including the plastic spin for plastically anisotropic materials are also investigated. Slightly promoted debonding was observed for $\theta_0 = 0°$ or 90°. However, if $\theta_0 = 22.5°$, 45° or 67.5° the plastic spin strongly promotes the failure by debonding. In particular, if plastic spin is accounted for using Barlat-91 with $\theta_0 = 45°$ the predicted failure strain is approximately half the failure strain if plastic spin is neglected, Figs. 5 and 9.

Effects of changing one of the boundary conditions from prescribing a shear stress to prescribing a shear deformation are also studied, Figs. 10 and 11. Since both conditions are fulfilled for isotropy and anisotropy with $\theta_0 = 0°$, 45° and 90°, only effects for $\theta_0 = 22.5°$ and 67.5° are observed, Fig. 10. In these cases, the quadratic yield function predicts a reduction in the failure strain from $\epsilon_1 \simeq 0.08$ to 0.06, and for the non-quadratic yield function the failure strain reduces from $\epsilon_1 \simeq 0.19$ to 0.11, Figs. 5 and 10.

The influence of plastic anisotropy on particle debonding is investigated in a generalized manner in this paper, due to the possibility of an arbitrary choice of θ_0. However, deformation dependent coefficients of anisotropy (anisotropic hardening) or other yield functions describing plastic anisotropy more accurately could also be considered. A flow criterion which is valid for full three-dimensional stress states has been proposed recently by Bron and Besson (2004). This yield function consists in a summation of a number of sub-functions each with individual powers, and the convexity of the yield criterion is guaranteed.

Acknowledgments

The author would like to thank Prof. Viggo Tvergaard, Technical University of Denmark for ideas, discussions and comments in order to realize this work. Assoc. Prof. Mitsutoshi Kuroda, Yamagata University, Japan, is thanked for providing some of the computer code used.

The work is financially supported by the Danish Technical Research Council in a project on Anisotropic Plasticity under the Materials Research Programme.

References

Bao, G., Hutchinson, J., McMeeking, R., 1991. Particle reinforcement of ductile matrices against plastic flow and creep. Acta Metallurgica et Materialia 39 (8), 1871–1882.

Barlat, F., Lege, D.J., Brem, J.C., 1991. A six-component yield function for anisotropic materials. International Journal of Plasticity 7, 693–712.

Barlat, F., Maeda, Y., Chung, K., Yanagawa, M., Brem, J.C., Hayashida, Y., Lege, D.J., Matsui, K., Murtha, S.J., Hattori, S., Becker, S., Makosey, S., 1997. Yield function development for aluminum alloy sheets. Journal of the Mechanics and Physics of Solids 45, 1727–1763.

Barlat, F., Brem, J.C., Yoon, J.W., Chung, K., Dick, R.E., Lege, D.J., Pourboghrat, F., Choi, S.-H., Chu, E., 2003. Plane stress yield function for aluminum alloy sheets—part I: theory. International Journal of Plasticity 19, 1297–1319.

Bron, F., Besson, J., 2004. A yield function for anisotropic materials. Application to aluminum alloys. International Journal of Plasticity 20, 937–963.

Christman, T., Needleman, A., Suresh, S., 1989a. An experimental and numerical study of deformation in metal–ceramic composites. Acta Metallurgica 37 (11), 3029–3050.

Christman, T., Needleman, A., Nutt, S., Suresh, S., 1989b. On microstructural evolution and micromechanical modelling of deformation of a whisker-reinforced metal–matrix composite. Materials Science and Engineering A 107 (1), 49–61.

Dafalias, Y.F., 1984. A missing link in the formulation and numerical implementation of finite transformation elastoplasticity. In: Willam, K. (Ed.), Constitutive Equations: Macro and Computational Aspects. ASME special publication, pp. 25–40.

Dafalias, Y.F., 1985a. A missing link in the macroscopic constitutive formulation of large plastic deformation. In: Sawczuk, A., Bianchi, G. (Eds.), Plasticity Today, Modelling, Methods and Applications. Elsevier, Amsterdam, pp. 135–151.

Dafalias, Y.F., 1985b. The plastic spin. Transactions of the ASME. Journal of Applied Mechanics 52 (4), 865–871.

Dafalias, Y.F., 1993. On multiple spins and texture development. Case study: kinematic and orthotropic hardening. Acta Mechanica 100, 171–194.

Dafalias, Y.F., 2000. Orientational evolution of plastic orthotropy in sheet metals. Journal of the Mechanics and Physics of Solids 48, 2231–2255.

Divecha, A.P., Fishman, S.G., Karmarkar, S.D., 1981. Silicon carbide reinforced aluminum—a formable composite. Journal of Metals 33, 12–17.

Hershey, A.V., 1954. The plasticity of an isotropic aggregate of anisotropic face centered cubic crystals. Transactions of the ASME. Journal of Applied Mechanics 21, 241–249.

Hill, R., 1948. A theory of the yielding and plastic flow of anisotropic metals. Proceedings of the Royal Society of London A 193, 281–297.

Hill, R., 1950. The Mathematical Theory of Plasticity. The Clarendon Press, Oxford.

Hosford, W.F., 1972. A generalized isotropic yield criterion. Transactions of the ASME. Series E, Journal of Applied Mechanics 39, 607–609.

Kuroda, M., 1995. Plastic spin associated with corner theory of plasticity. International Journal of Plasticity 11, 547–570.

Kuroda, M., 1996. Roles of plastic spin in shear banding. International Journal of Plasticity 12, 671–693.

Kuroda, M., 1997. Interpretation of the behavior of metals under large plastic shear deformation: a macroscopic approach. International Journal of Plasticity, 359–383.

Kuroda, M., 1999. Interpretation of the behavior of metals under large plastic shear deformations: comparison of macroscopic predictions to physically based predictions. International Journal of Plasticity, 1217–1236.

Legarth, B.N., 2003. Debonding of particles in anisotropic materials. International Journal of Mechanical Sciences 45, 1119–1133.

Legarth, B.N., Kuroda, M., in press. Particle debonding using different yield criteria. European Journal of Mechanics A/Solids.

Legarth, B.N., Tvergaard, V., Kuroda, M., 2002. Effects of plastic anisotropy on crack-tip behaviour. International Journal of Fracture 117, 297–312.

Levitas, V., 1998. A new look at the problem of plastic spin based on stability analysis. Journal of the Mechanics and Physics of Solids 46, 557–590.

Logan, R.W., Hosford, W.F., 1980. Upper-bound anisotropic yield locus calculations assuming $\langle 1\,1\,1 \rangle$-pencil glide. International Journal of Mechanical Sciences 22, 419–430.

McDanels, D., 1985. Analysis of stress–strain, fracture, and ductility behavior of aluminum matrix composites containing discontinuous silicon carbide reinforcement. Metallurgical Transactions A (Physical Metallurgy and Materials Science) 16A (6), 1105–1115.

McMeeking, R.M., Rice, J.R., 1975. Finite-element formulations for problems of large elastic–plastic deformation. International Journal of Solids and Structures 11, 601–616.

Needleman, A., 1987. A continuum model for void nucleation by inclusion debonding. Journal of Applied Mechanics 54, 525–531.

Niordson, C.F., Tvergaard, V., 2002. Nonlocal plasticity effects on fibre debonding in a whisker-reinforced metal. European Journal of Mechanics A/Solids 21 (2), 239–248.

Nutt, S., Needleman, A., 1987. Void nucleation at fiber ends in Al–SiC composites. Scripta Metallurgica 21, 705–710.

Peirce, D., Shih, C., F, Needleman, A., 1984. A tangent modulus method for rate dependent solids. Computers and Structures 18, 875–887.

Tvergaard, V., 1976. Effect of thickness inhomogeneities in internally pressurized elastic–plastic spherical shells. Journal of the Mechanics and Physics of Solids 24, 291–304.

Tvergaard, V., 1990a. Analysis of tensile properties for a whisker-reinforced metal–matrix composite. Acta Metallurgica 38 (2), 185–194.

Tvergaard, V., 1990b. Effect of fibre debonding in a whisker-reinforced metal. Materials Science and Engineering A 125, 203–213.

Tvergaard, V., 1995. Fibre debonding and breakage in a whisker-reinforced metal. Materials Science and Engineering A 190, 215–222.

Xu, X.-P., Needleman, A., 1993. Void nucleation by inclusion debonding in a crystal matrix. Modelling and Simulation in Materials Science and Engineering 1, 111–132.

Yamada, Y., Hirakawa, H., 1978. Large deformation and instability analysis in metal forming process. Applications of Numerical Methods to Forming Processes, ASME, AMD 28, 27–38.

Yamada, Y., Sasaki, M., 1995. Elastic–plastic large deformation analysis program and lamina compression test. International Journal of Mechanics, 691–707.

Zbib, H.M., Aifantis, E., 1988. On the concept of relative and plastic spins and its implications to large deformation theories. Part I and II. Acta Mechanica 75 (15–33), 35–56.